Hydrogen-on-Demand Using Metallic Alloy Nanoparticles in Water

Kohei Shimamura,[†,‡,§,∥,⊥] Fuyuki Shimojo,[†,‡,§,∥,⊥] Rajiv K. Kalia,[†,‡,§,∥] Aiichiro Nakano,*[,†,‡,§,∥] Ken-ichi Nomura,[†,‡,§,∥] and Priya Vashishta[†,‡,§,∥]

[†]Collaboratory for Advanced Computing and Simulations, [‡]Department of Physics and Astronomy, [§]Department of Computer Science, and [∥]Department of Chemical Engineering and Materials Science, University of Southern California, Los Angeles, California 90089-0242, United States

[⊥]Department of Physics, Kumamoto University, Kumamoto 860-8555, Japan

S Supporting Information

ABSTRACT: Hydrogen production from water using Al particles could provide a renewable energy cycle. However, its practical application is hampered by the low reaction rate and poor yield. Here, large quantum molecular dynamics simulations involving up to 16 611 atoms show that orders-of-magnitude faster reactions with higher yields can be achieved by alloying Al particles with Li. A key nanostructural design is identified as the abundance of neighboring Lewis acid−base pairs, where water-dissociation and hydrogen-production require very small activation energies. These reactions are facilitated by charge pathways across Al atoms that collectively act as a "superanion" and a surprising autocatalytic behavior of bridging Li−O−Al products. Furthermore, dissolution of Li atoms into water produces a corrosive basic solution that inhibits the formation of a reaction-stopping oxide layer on the particle surface, thereby increasing the yield. These atomistic mechanisms not only explain recent experimental findings but also predict the scalability of this hydrogen-on-demand technology at industrial scales.

KEYWORDS: Hydrogen on demand, LiAl nanoparticle, water, quantum molecular dynamics
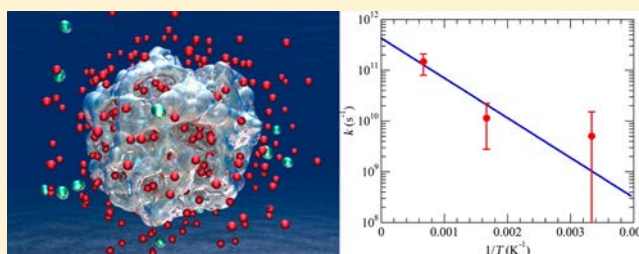
Metals such as Al can be used in renewable energy cycles.[1] In a two-step thermochemical cycle, an exothermic reaction between metal and water produces hydrogen gas, followed by endothermic reduction of the metal-oxide product assisted by solar energy to regenerate metal fuel.[1−3] One potential application of this technology is on-board hydrogen production for hydrogen-powered vehicles, but conventional metal−water reaction kinetics is not fast enough to make such on-demand hydrogen production commercially viable.[4] Previous experimental[5] and theoretical[5,6] works suggested that remarkable reactivity of "superatoms"[7−10] (i.e., clusters consisting of a magic number of Al atoms) with water may solve this problem. A pioneering experiment by Castleman's group demonstrated size-selective reactivity of Al clusters, Al_n^- (e.g., n = 12 or 17), with water molecules in gas phase.[5] Quantum-mechanical calculation by Khanna's group suggested that complementary pairs of Lewis acid and base sites on an Al superatom surface preferentially accelerate hydrogen production.[5] In a small cluster, geometrical arrangement is not identical for all surface atoms. Consequently, some surface Al atoms act as Lewis acid and others as Lewis base. Spatially proximate pairs of Lewis acid and base sites on a superatom surface feature low activation barriers for H_2 production.[5,6] Subsequent quantum molecular dynamics (QMD) simulation demonstrated accelerated hydrogen production from liquid water using Al superatoms.[6] The simulation results revealed a

reaction mechanism with a much lower activation barrier than in gas phase. This reaction, which also occurs at Lewis acid−base pairs, is further accelerated by rapid proton transport in water via a chain of hydrogen-bond switching events. This Grotthuss mechanism[11] converts hydroxide ions to water molecules at Lewis-acid sites and supplies hydrogen atoms to Lewis-base sites.

While this superatomic design achieves high reaction rates in nanometer-size clusters, unfortunately, it does not scale up to larger particle sizes of industrial relevance. For larger particles, surface atoms begin to lose acid−base distinction that originates from local geometrical differences on nanocluster surfaces. More seriously, formation of an inert oxide or hydroxide layer associated with the hydrogen-production reaction protects the metal core and thereby stops the reaction incomplete. This leaves a large fraction of Al atoms unreacted, leading to low yields.[12−14] Radically new design principles are thus needed for scalable high-yield H_2 production. Recent experiments showed that alloying (e.g., with Li[15−17] or Ga−In−Sn[18]) often results in 100% yield for hydrogen production, which can potentially solve the low-yield problem of Al
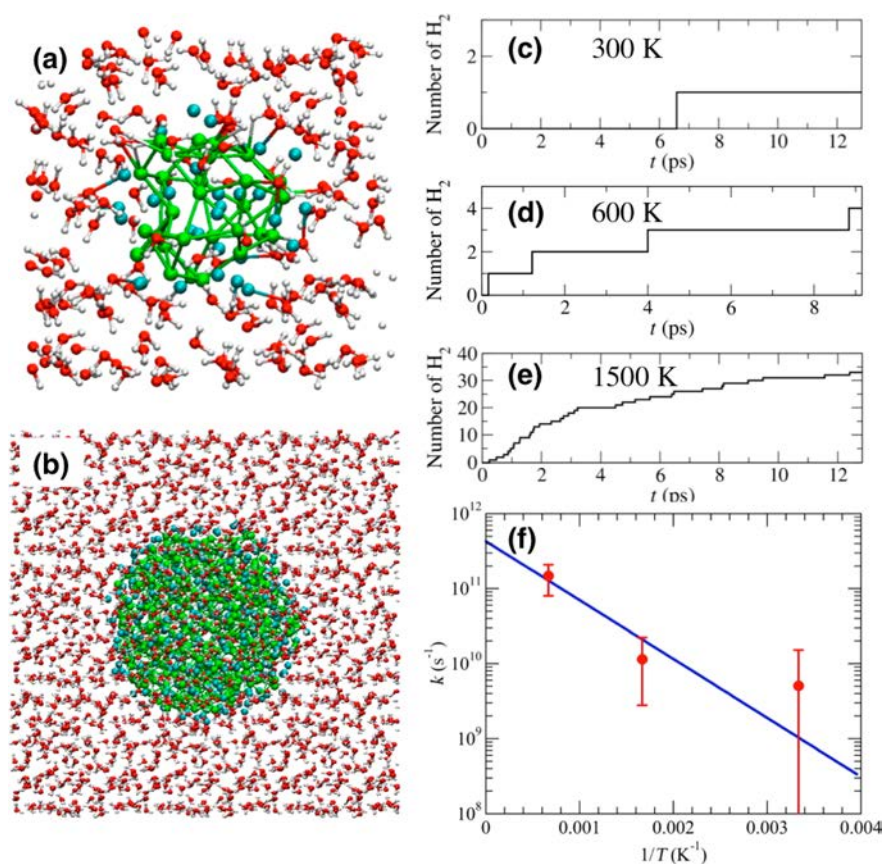
Figure 1. Rapid H_2 production from water using Li_nAl_n particles. Initial configurations for the (a) 606-atom and (b) 16 611-atom systems, where cyan, green, white, and red spheres represent Li, Al, H, and O atoms, respectively. (c−e) The number of produced H_2 molecules as a function of time at temperatures of 300 K (c), 600 K (d), and (e) 1500 K for $n = 30$. (f) Hydrogen production rate as a function of temperature (red circles with error bars), where the blue line is the best fit to the Arrhenius equation.

particles. However, atomistic mechanisms for the observed high reactivity and yield due to alloying remain elusive.

Elucidating atomistic mechanisms of hydrogen production would require large QMD simulations involving tens of thousands of atoms, which follow the trajectories of all atoms while computing interatomic forces quantum mechanically from first principles.[19,20] This year marks the 50th anniversary of two seminal developments that underpin the QMD method: The first molecular dynamics simulation using empirical interatomic forces by Aneesur Rahman;[21] and introduction of the density functional theory (DFT,)[22] the most widely used quantum mechanical method, for which Walter Kohn received a Nobel chemistry prize in 1998. By solving N one-electron problems self-consistently instead of directly solving one N-electron problem, DFT approximately reduces the exponential complexity of solving the quantum N-body problem to $O(N^3)$. DFT-based QMD simulations are typically limited to small systems involving a few hundred atoms due to the asymptotic $O(N^3)$ computational complexity. To overcome this bottleneck, various $O(N)$ DFT algorithms[23] have been designed on the basis of the locality principle called quantum nearsightedness[24] in which the computation time scales only linearly with the number of electrons. Among them, the divide-and-conquer (DC) DFT algorithm pioneered by Weitao Yang[25] is highly scalable on massively parallel supercomputers. With recent improvements, the DC-DFT algorithm has at last attained controlled error bounds, robust convergence properties, and adequate energy conservation for its use in QMD simulations,

thereby making large DC-DFT-based QMD simulations practical.[26]

Rapid Hydrogen Production. We performed large QMD simulations on a parallel supercomputer consisting of 786 432 processors (see Supporting Information for simulation methods) to provide spatially and temporally resolved reaction dynamics of Li_nAl_n particles at the atomic resolution ($n = 30$, 135, and 441); see Figure 1a,b. In each case, a spherical particle is cut out from the LiAl crystal with the Zintl structure,[27] which is then immersed in bulk water. The total numbers of atoms involved in the simulation are 606, 4836 and 16 611, respectively, for the $Li_{30}Al_{30}$, $Li_{135}Al_{135}$, and $Li_{441}Al_{441}$ systems (see the movie file in the Supporting Information for the 16 611-atom QMD simulation). Figure 1c−e shows the number of H_2 molecules produced during QMD simulations at different temperatures for $Li_{30}Al_{30}$. A total of 1, 4, and 19 H_2 molecules were produced from water using $Li_{30}Al_{30}$ within 10 ps at temperatures 300, 600, and 1500 K, respectively. The reaction rate here is drastically higher than Al_n (n is between 12 and 55), for which no H_2 production was observed at 300 and 600 K within a similar time frame.[6,28,29] To estimate the reaction rate, we analyzed the distribution of the time interval between consecutive H_2 productions. We found that the reaction time follows the Poisson distribution from which the reaction rate was extracted. Supporting Information, Figure S1 shows the close agreement of the calculated distribution of the reaction time interval with the Poisson distribution. Figure 1f plots the normalized H_2 production rate per LiAl pair as a function of
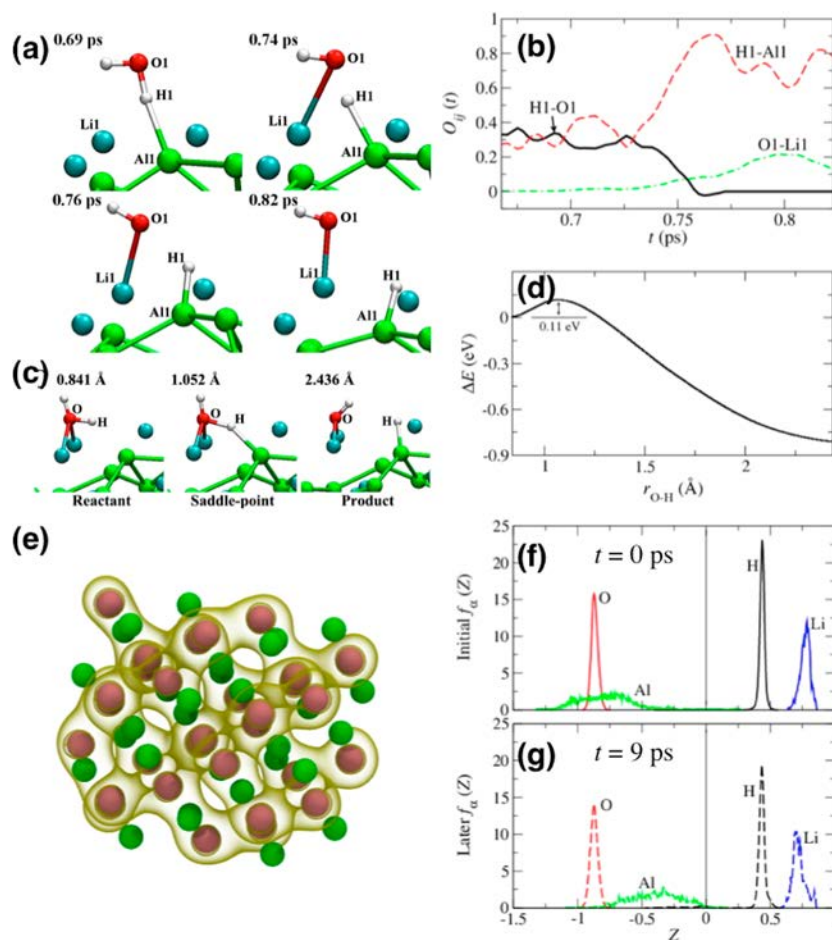
Figure 2. Atomistic mechanisms of rapid H_2O dissociation on a $Li_{30}Al_{30}$ surface. (a) H_2O dissociates at a complementary pair of Lewis acid (Li1) and base (Al1) sites. Here, cyan, green, white, and red spheres are Li, Al, H, and O atoms, respectively. (b) Time evolution of Mulliken bond-overlap populations for key atomic pairs involved in the reaction. (c) Reactant, saddle-point and product states for the water dissociation reaction. The numerals denote the distance between the O and H atoms marked in the figure. (d) Energy as a function of the reaction coordinate (O−H distance) of the water dissociation reaction. (e) Zintl superatomic alloy architecture for hydrogen production, where magenta and green spheres are Al and Li atoms and an isosurface of the electron charge density is shown in yellow. (f,g) Atomic charge distribution at times 0 (f) and 9 ps (g) of the 600 K simulation.

temperature T. We fitted the calculated rates to the Arrhenius relation, $k(T) = k_0 \exp(-\Delta/k_B T)$, where Δ is the activation barrier, k_B is the Boltzmann constant, and k_0 is a constant. The best fit yields $\Delta = 0.0676$ eV. This is an order-of-magnitude lower than the calculated activation barrier of 0.3 eV for H_2 production from water using Al nanoparticles, where the water-splitting reaction was the rate limiting process.[6,28,29] The estimated H_2 production rate from this fit is 1.04×10^9 s^{-1} at 300 K, which is much higher than 10^7 s^{-1} for Al_n.[6,28,29] The simulation results thus demonstrate a dramatically accelerated reaction of Li-alloyed Al particles compared with pure Al particles for producing hydrogen from water.

Rapid Water-Dissociation Mechanism. To understand the atomistic mechanisms underlying the rapid H_2 production from water using Li_nAl_n particles shown above, we analyzed atomic trajectories during the simulation. The first step in H_2 production is the dissociation of a H_2O molecule to produce H and hydroxyl (OH) groups on the metallic particle surface, which was found to be the rate-limiting process for H_2 production from water using Al particles.[6,28,29] Figure 2a shows snapshots of one of the H_2O dissociation events for $Li_{30}Al_{30}$ at a temperature of 600 K. Here, the H_2O molecule dissociates at neighboring Li and Al sites

$$Li\text{-}OH_2 + Al \rightarrow Li\text{-}OH + Al\text{-}H \tag{1}$$

While a surface Al atom (labeled Al1) attracts H (labeled H1) in a water molecule, a neighboring Li atom (labeled Li1) attracts O (labeled O1) and thereby weakens the O1−H1 bond. This leads to the dissociation of the O1−H1 bond and concomitant formation of the Al1−H1 bond. To quantify this reaction, we performed bond-overlap population (BOP) analysis (see Supporting Information). Figure 2b plots the time evolution of the BOP values O_{ij} between key atomic pairs i and j involved in the reaction in Figure 2a. We observe that O_{H1-O1} decreases while O_{H1-Al1} increases at ∼0.75 ps.

To estimate the energy barrier for the water dissociation reaction, we performed a nudged elastic band (NEB) calculation for the reaction represented by eq 1 in a simpler system without surrounding water molecules as shown in Figure 2c. Here, the left, center, and right images are the initial (or reactant), saddle-point and final (or product) states of the reaction, respectively. Figure 2d shows the calculated energy profile along the reaction coordinate, which is the distance between the O−H bond within H_2O to be broken by this reaction. The calculated activation barrier (0.11 eV) in Figure 2d is much lower than that (0.3 eV) for pure Al_n cluster.[6,28,29]
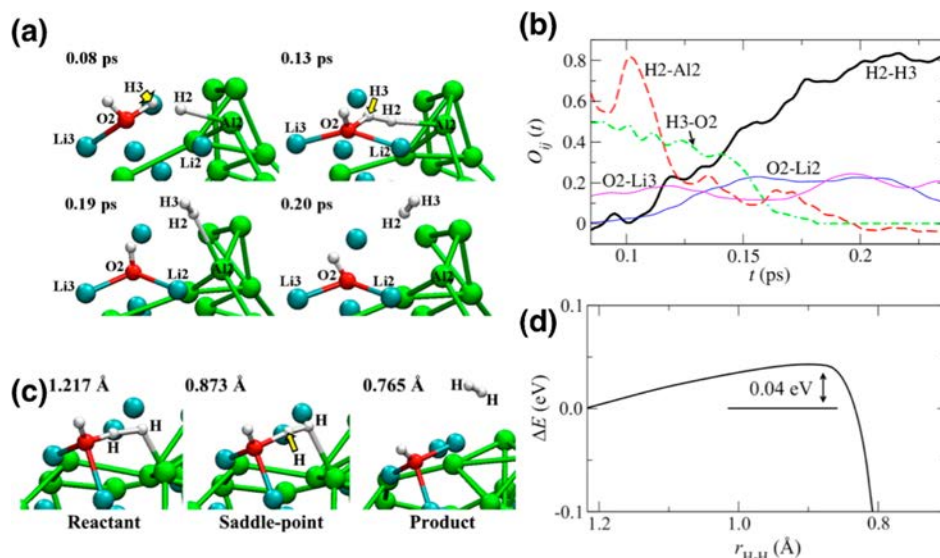
Figure 3. Atomistic mechanisms of rapid H_2 production on a $Li_{30}Al_{30}$ surface. (a) H_2 production at a Lewis acid (labeled Li2) and base (Al2) pair. (b) Time evolution of bond-overlap populations for key atom pairs involved in the reaction. (c) Initial (or reactant), saddle-point, and final (or product) states for a H_2 production reaction. The numerals denote the distance between the two H atoms that form the H_2 product. (d) Energy as a function of the reaction coordinate (H–H distance) of the H_2 production reaction.

This activation barrier is consistent with, but slightly higher than, the activation barrier (0.068 eV) for the overall H_2 production rate estimated from Figure 1. This is likely due to the surrounding bulk water present in the latter but not in the former case. Such solvation shells were shown to lower the activation barrier significantly.[29] Here, it is worth noting that the weakening of an intrawater O–H bond is caused by the formation of a Li–O bond (see Li1–O1 in Figure 2a,b).

The above analysis shows that key to the rapid H_2O dissociation reaction is the presence of a complementary pair of Lewis acid (Li) and base (Al) sites, which respectively produce OH and H groups. Similar complementary acid–base pairs were also found to accelerate H_2O dissociation using Al_n.[5,6,28,29] In the case of Al_n, however, these complementary pairs are a consequence of different local geometric arrangements of atoms in nanoparticles. Because all Al atoms are chemically equivalent, the number density of these geometrically induced acid–base pairs and their strengths are rather low. In contrast, the Zintl crystal structure of LiAl is understood as interleaved diamond sublattices of Li and Al,[27] and consequently complementary pairs of Li acid and Al base sites are abundant on the surface of a Li_nAl_n particle (see Figure 2e). Here, the nature of this complementary pairs is intrinsic to the crystal structure. In the LiAl crystal, charge transfer from Li to Al makes the valence charge to be predominantly distributed around Al atoms. Thus, Li_nAl_n with the Zintl crystalline structure behaves as a compound of an Al_n^{n-} superanion dispersed with Li^+ cations. In fact, the electronic charge density in Figure 2e shows that the electrons are extended throughout the Al sublattice. Consequently, the charge of an individual Al atom is not a good quantum number. Accordingly, the histogram of atomic charges for Al atoms in Figure 2f at time $t = 0$ exhibits a broad distribution. In contrast, Li atoms in the Zintl-crystalline particle donate electrons to Al and becomes Li^+ (Figure 2e). These Li^+ ions are isolated from each other, and accordingly their charge histogram in Figure 2f is sharply peaked. Thus, in a Zintl LiAl particle, the diamond-structured Al sublattice is metallically bonded. This Al superanion in turn is bonded with

individual Li ions ionically. These key features of charge distribution remain unchanged until the end of the simulation (see Figure 2g). Because of the charge transfer from Li to Al atoms, Li levels near the Fermi energy are largely unoccupied, facilitating their roles as electron acceptors (or Lewis acid). On the other hand, Al levels near the Fermi energy are highly occupied, making them electron donors (or Lewis base). Supporting Information, Figure S2 shows electronic partial densities of states projected onto Al and Li atoms to quantify this difference. This Zintl superatomic architecture is essential for the high reactivity of LiAl alloy particles with water. The electronic structures of similar Al Zintl anion moieties in NaAl clusters have recently been studied by electronic structure calculations.[30]

Proton Transport. According to our previous QMD simulations, a hydroxyl group created at a Lewis acid site on metal surface immersed in bulk water can be rapidly converted back to H_2O. This reaction occurs nearly barrierless, which is assisted by a chain of hydrogen-bond switching events similar to the Grotthuss mechanism.[6,28,29] In the present simulation, we also observed the conversion of Li–OH back to $Li–OH_2$

$$Li\text{-}OH + H_2O \rightarrow Li\text{-}OH_2 + OH \qquad (2)$$
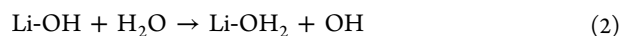
We found a large number of Grotthuss proton-transfer events even in the 300 K simulation, indicating rapid proton exchange reactions, eq 2, with extremely low activation-barriers (see the number of Grotthuss events as a function of time in Supporting Information, Figure S3). As explained above, Li_nAl_n features abundant pairs of adjacent complementary Lewis acid (Li) and base (Al) pairs for low activation-barrier water splitting. In addition, as we have also shown, the Al superanion provides a continuous charge-transfer network, which, together with the Grotthuss proton transport in water, facilitates rapid H_2 production.

Rapid H_2 Production Mechanism. As a result of the water-dissociation reaction, eq 1, and the proton-exchange reaction, eq 2, there exist a large number of H_2O molecules adsorbed on Li sites as well as H atoms adsorbed on neighboring Al sites on the Li_nAl_n surface. We observed the
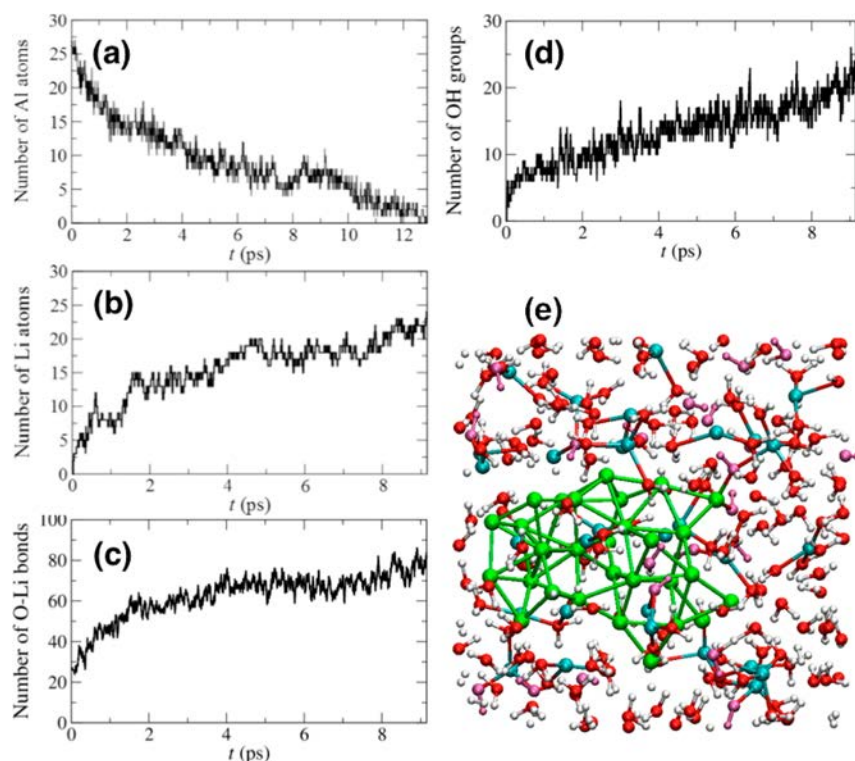
Figure 4. High-yield H_2 production from water using $Li_{30}Al_{30}$. (a) The number of unreacted Al atoms as a function of time at 1500 K. (b) Time evolution of the number of Li atoms that are not bonded to Al at 600 K. (c) The number of O−Li bonds as a function of time in the same simulation. (d) The number of OH groups as a function of time. (e) Spatial distribution of OH groups (magenta) in a snapshot at 600 K.

production of H_2 molecules at these complementary Lewis acid−base sites. Among various H_2 production reactions is

$$Li\text{-}OH_2 + Al\text{-}H \rightarrow Li\text{-}OH + Al + H_2 \qquad (3)$$
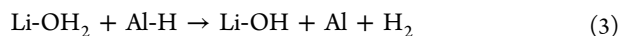
Figure 3a shows snapshots of one of these reactions on $Li_{30}Al_{30}$ at 600 K. Figure 3b shows the time evolution of Mulliken BOPs for key atomic pairs involved in this reaction. We see the decrease of O_{H2-Al2} around 0.12 ps, indicating the breakage of the Al−H bond. This is accompanied by the increase of O_{H2-H3} due to the formation of the H_2 product.

To estimate the energy barrier for the H_2 production reaction, we performed a NEB calculation for the reaction represented in a simpler system shown in Figure 3c without surrounding water molecules. Here, the left, center, and right images are the reactant, saddle-point, and product states, respectively. Figure 3d shows the calculated energy profile along the reaction coordinate, which is the distance between the two H atoms that form the H_2 product. The calculated activation barrier (0.04 eV) in Figure 3d is much lower than that (0.11 eV) for the water dissociation reaction in Figure 2. Thus, the latter is the rate-limiting step for H_2 production from water using Li_nAl_n. We should note that the activation energy calculated here (0.04 eV) is much lower than that (0.1 eV) for the H_2-production reaction on Al_n surface.[6,28,29] The stronger Lewis acid (Li)-base (Al) pairs may explain the faster H_2 production from water using Li_nAl_n instead of Al_n. This mechanism explains the experimentally observed alloy composition-dependence of the reaction speed for H_2 production from water using Li_xAl_{1-x} alloy particles.[17] Namely, the observed reaction speed is an increasing function of x up to $x = 0.5$. This is consistent with the increased number of Lewis acid−base pairs as a function of x in the range [0, 0.5].

From the NEB calculations, we also calculated the energy generated by each exothermic H_2 production to be 2.3 eV. To study how the resulting heat affects the reaction rate, let us consider the case of $Li_{30}Al_{30}$, for which the mean time interval between successive H_2 productions was estimated to be $\tau = 32$ ps at 300 K. With a typical thermal diffusivity of $D = 10^{-4}$ (m^2/s) for metal, the corresponding thermal diffusion length is $L = (D\tau)^{1/2} \sim 60$ nm. This is larger than the diameter of the $Li_{30}Al_{30}$ particle, 1.4 nm. Consequently, the entire LiAl particle heats up uniformly between consecutive H_2 productions. Though the thermal diffusivity of water ($\sim 10^{-7}$ m^2/s) and the corresponding thermal diffusion length (~ 2 nm) are much smaller, a thin water layer of thickness 2 nm also heats up to the same temperature. By dividing the generated energy of 2.3 eV by the total number of atoms in the water-coated $Li_{30}Al_{30}$ particle, 6400, we obtain the energy gain by each atom to be 4 × 10^{-4} eV or the corresponding temperature increase of 4 K. At lower temperatures, this temperature increase slightly enhances the probability to overcome the activation barrier and accordingly the reaction rate. Because of the decreasing surface-to-volume ratio, however, this effect is far less significant for larger particles.

High-Yield H_2 Production Mechanism. A major problem for H_2 production from water using Al particles is its low yield. Because of the formation of a passive oxide or hydroxide coating layer on the particle surface, reaction of the inner Al core with water becomes prohibited and the Al core remains unreacted.[31] In contrast, we here found a high yield of H_2 production reactions from water using Li_nAl_n particles. Figure 4a shows the number of unreacted Al atoms for $Li_{30}Al_{30}$ at 1500 K as a function of time. Here, an unreacted Al atom is defined as that only bonded to other Al atoms. At the end of the simulation, no Al atom remains unreacted. This is in contrast to

Al_n in water at 1500 K in which most inner Al atoms in the particle remained intact.[6,28,29]

To understand the atomistic mechanism of the high-yield H_2 production, Figure 4b plots the time evolution of the number of Li atoms that are not bonded to Al during the $Li_{30}Al_{30}$ simulation at a temperature of 600 K. Also shown in Figure 4c is the number of O—Li bonds as a function of time in the same simulation. More and more Li atoms get bonded to O from water as time progresses. At the same time, a decreasing number of Li atoms remain bonded to Al. This is understandable because each water molecule has two lone-pair electrons, and it acts as a stronger electron donor to a Li atom than an Al atom does.

To study the oxidation dynamics, Supporting Information, Figure S4a shows the time evolution of the number of bridging oxygens, Al—O—Al, Al—O—Li, and Li—O—Li, in the $Li_{30}Al_{30}$ system at 1,500 K. Both Al—O—Li and Li—O—Li appear immediately starting at time 0, with Al—O—Li being the dominant reaction product. In contrast, delayed production of Al—O—Al starts only after a latent time of ~3 ps. To understand the nature of these bridging oxygens,[32] Supporting Information, Figure S4b plots the same quantity as Supporting Information, Figure S4a but including only those bonds that continuously exist longer than a minimum bond lifetime of 0.484 ps. The results show that only Al—O—Al groups are stable reaction products, while Al—O—Li and Li—O—Li are continuously formed and broken. Namely, bridging oxygens that connect Al and Li are not merely inert reaction products but instead play an active role in the oxidation process by assisting the breakage of O—H (Supporting Information, Figure S5a) and formation of Al—O (Supporting Information, Figure S5b) bonds. Similar catalytic behavior of reaction products was found during the detonation of pentaerythritol tetranitrate ($C_5H_8N_4O_{12}$), where H_2O products are directly involved in the breakage of N—O and formation of C—O bonds.[33]

We also found that the LiOH product of the water dissociation reaction at the acidic Li site on surface (see eq 1) dissolves quickly into water. Figure 4d shows the number of OH groups produced in the $Li_{30}Al_{30}$ system at 600 K. We see a continuous increase in the number of hydroxides. In the snapshot of the same simulation in Figure 4e, isolated OH fragments colored in magenta show that a large number of OH groups in fact dissolved into water. Supporting Information, Figure S6 shows the radial density profiles of Al (solid black line), Li (solid red line), and OH^- (dashed cyan line) in the $Li_{441}Al_{441}$ system at 1500 K at the end of the simulation, where the radius r is the distance from the center-of-mass of the $Li_{441}Al_{441}$ particle. We observe the spreading of Li and OH^- to larger r values (i.e., into water). The increased OH^- density in water associated with Li dissolution explains recent experimental observation that the reaction of Li_xAl_{1-x} alloy particles with water produces basic solution and that the resulting pH value is an increasing function of the Li composition, x.[17] The locally basic solution is likely the key mechanism of high yield. It is well-known that basic solutions such as NaOH corrode the passive oxide layer of Al and consequently even household Al foils react completely with water to produce hydrogen gas.[34] In addition, the leaching of Li atoms into water leaves behind voids to form a lower density Al-rich particle. This in turn provides pathways through which water continues to react with Al and remaining Li atoms. The dissolution of Li atoms into water is driven by its stronger bonding with water molecules than with Al and is assisted by high mobility of Li atoms. This is

reflected in the larger mean square displacement of Li atoms as compared to that of Al atoms shown in Supporting Information, Figure S7.

It is worth noting that Al atoms become less negatively charged as the reaction with water progresses (see Figure 2g at 9 ps in the $Li_{30}Al_{30}$ simulation at 600 K). This reflects the overall H_2 production[17]

$$2LiAl + 8H_2O \rightarrow LiAl_2(OH)_7 + LiOH + 4H_2 \qquad (4)$$
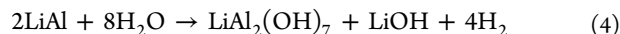
In an unreacted LiAl particle with the Zintl crystalline structure, charge transfer from Li to Al atoms make the latter negatively charged (see Figure 2f). In the $LiAl_2(OH)_7$ product, however, some of the Al charge is transferred to O atoms and makes Al less negatively charged (Figure 2g).

Scalability of the Technology. A serious problem about H_2 production from water using Al particles is the lack of scalability. Namely, the high reactivity of Al nanoparticles cannot be sustained for larger particles that are commercially mass-produced. To investigate the scalability of the high reactivity of Li_nAl_n with water, we performed simulations involving larger particles, $Li_{135}Al_{135}$ and $Li_{441}Al_{441}$, in water at 1500 K. Supporting Information, Figure S8a shows the number of produced H_2 molecules as a function of time. More H_2 molecules are generated by $Li_{441}Al_{441}$ than by $Li_{135}Al_{135}$. Supporting Information, Figure S8b plots the H_2 production rate normalized by the number of surface atoms, N_{surf}, as a function of N_{surf} for the three systems. Here, the surface atoms are defined as those with lower coordination numbers than the bulk value. The normalized H_2 production rate is constant as a function of N_{surf} within error bars. The size effect is thus negligible, indicating that the Li_nAl_n surface is equally reactive regardless of the surface curvature. Thus, the Zintl design for H_2 production proposed here is expected to scale up to industrially relevant particle sizes. Not only does this microscopic understanding explains recent experimental findings in similar alloy systems (e.g., alloy composition-dependent reactivity and a remarkable pH change associated with H_2 production),[17] but it also predicts a scalable nanostructural design for rapid high-yield production of hydrogen on demand.

ASSOCIATED CONTENT

Ⓢ Supporting Information
Technical details of the QMD simulation methods and additional figures. This material is available free of charge via the Internet at http://pubs.acs.org.

AUTHOR INFORMATION

Corresponding Author
*E-mail: anakano@usc.edu.

Author Contributions
F.S., A.N., R.K.K., and P.V. designed the research. K.S. performed QMD simulations, and K.N. performed larger QMD simulation on Blue Gene/Q. All participated in data analysis and writing the paper.

Notes
The authors declare no competing financial interest.

■ REFERENCES

(1) Muhich, C. L.; Evanko, B. W.; Weston, K. C.; Lichty, P.; Liang, X. H.; Martinek, J.; Musgrave, C. B.; Weimer, A. W. *Science* **2013**, *341* (6145), 540−542.

(2) Steinfeld, A. *Sol. Energy* **2005**, *78* (5), 603−615.

(3) Chueh, W. C.; Falter, C.; Abbott, M.; Scipio, D.; Furler, P.; Haile, S. M.; Steinfeld, A. *Science* **2010**, *330* (6012), 1797−1801.

(4) Petrovic, J.; Thomas, G. *Reaction of Aluminum with Water to Produce Hydrogen*; U.S. Department of Energy: Washington, DC, 2008.

(5) Roach, P. J.; Woodward, W. H.; Castleman, A. W.; Reber, A. C.; Khanna, S. N. *Science* **2009**, *323* (5913), 492−495.

(6) Shimojo, F.; Ohmura, S.; Kalia, R. K.; Nakano, A.; Vashishta, P. *Phys. Rev. Lett.* **2010**, *104* (12), 126102.

(7) Khanna, S. N.; Jena, P. *Phys. Rev. Lett.* **1992**, *69* (11), 1664−1667.

(8) Khanna, S. N.; Jena, P. *Phys. Rev. B* **1995**, *51* (19), 13705−13716.

(9) Bergeron, D. E.; Castleman, A. W.; Morisato, T.; Khanna, S. N. *Science* **2004**, *304* (5667), 84−87.

(10) Jena, P.; Castleman, A. W. *Proc. Natl. Acad. Sci. U.S.A.* **2006**, *103* (28), 10560−10569.

(11) Agmon, N. *Chem. Phys. Lett.* **1995**, *244* (5−6), 456−462.

(12) Deng, Z. Y.; Ferreiraw, J. M. F.; Tanaka, Y.; Ye, J. H. *J. Am. Ceram. Soc.* **2007**, *90* (5), 1521−1526.

(13) Risha, G. A.; Son, S. F.; Yetter, R. A.; Yang, V.; Tappan, B. C. *Proc. Combust. Inst.* **2007**, *31* (2), 2029−2036.

(14) Conner, R. W.; Dlott, D. D. *Chem. Phys. Lett.* **2011**, *512* (4−6), 211−216.

(15) Rosenband, V.; Gany, A. *Int. J. Hydrogen Energy* **2010**, *35* (20), 10898−10904.

(16) Lin, M. C.; Uan, J. Y.; Tsai, T. C. *Int. J. Hydrogen Energy* **2012**, *37* (18), 13731−13736.

(17) Chen, X.; Zhao, Z.; Hao, M.; Wang, D. *Int. J. Energy Res.* **2013**, *37* (13), 1624−1634.

(18) Ziebarth, J. T.; Woodall, J. M.; Kramer, R. A.; Choi, G. *Int. J. Hydrogen Energy* **2011**, *36* (9), 5271−5279.

(19) Car, R.; Parrinello, M. *Phys. Rev. Lett.* **1985**, *55* (22), 2471−2474.

(20) Payne, M. C.; Teter, M. P.; Allan, D. C.; Arias, T. A.; Joannopoulos, J. D. *Rev. Mod. Phys.* **1992**, *64* (4), 1045−1097.

(21) Rahman, A. *Phys. Rev.* **1964**, *136* (2A), A405−A411.

(22) Hohenberg, P.; Kohn, W. *Phys. Rev.* **1964**, *136* (3B), B864−B871.

(23) Bowler, D. R.; Miyazaki, T. *Rep. Prog. Phys.* **2012**, *75* (3), 036503.

(24) Prodan, E.; Kohn, W. *Proc. Natl. Acad. Sci. U.S.A.* **2005**, *102* (33), 11635−11638.

(25) Yang, W. T. *Phys. Rev. Lett.* **1991**, *66* (11), 1438−1441.

(26) Shimojo, F.; Kalia, R. K.; Kunaseth, M.; Nakano, A.; Nomura, K.; Ohmura, S.; Shimamura, K.; Vashishta, P. *J. Chem. Phys.* **2014**, *140* (18), 18A529.

(27) Guo, X. Q.; Podloucky, R.; Freeman, A. J. *Phys. Rev. B* **1989**, *40* (5), 2793−2800.

(28) Ohmura, S.; Shimojo, F.; Kalia, R. K.; Kunaseth, M.; Nakano, A.; Vashishta, P. *J. Chem. Phys.* **2011**, *134* (24), 244702.

(29) Mou, W.; Ohmura, S.; Hemeryck, A.; Shimojo, F.; Kalia, R. K.; Nakano, A.; Vashishta, P. *AIP Adv.* **2011**, *1* (4), 042149.

(30) Wang, H. P.; Zhang, X. X.; Ko, Y. J.; Grubisic, A.; Li, X.; Gantefor, G.; Schnockel, H.; Eichhorn, B. W.; Lee, M. S.; Jena, P.; Kandalam, A. K.; Kiran, B.; Bowen, K. H. *J. Chem. Phys.* **2014**, *140* (5), 054301.

(31) Campbell, T. J.; Kalia, R. K.; Nakano, A.; Vashishta, P.; Ogata, S.; Rodgers, S. *Phys. Rev. Lett.* **1999**, *82* (24), 4866−4869.

(32) Liang, T.; Sawyer, W. G.; Perry, S. S.; Sinnott, S. B.; Phillpot, S. R. *J. Phys. Chem. C* **2011**, *115* (21), 10606−10616.

(33) Wu, C. J.; Fried, L. E.; Yang, L. H.; Goldman, N.; Bastea, S. *Nature Chem.* **2009**, *1* (1), 57−62.

(34) Wang, H. Z.; Leung, D. Y. C.; Leung, M. K. H.; Ni, M. *Renewable Sustainable Energy Rev.* **2009**, *13* (4), 845−853.